Determination of the Rate Constant for the Radical−Radical Reaction NCO($X^2\Pi$) + CH_3(X^2A_2'') at 293 K and an Estimate of Possible Product Channels

Yide Gao[†] **and R. Glen Macdonald***

Chemistry Division, Argonne National Laboratory, 9700 South Cass Avenue, Argonne, Illinois 60439-4831

Received: September 6, 2005

The rate constant for the reaction of the cyanato radical, NCO($X^2\Pi$), with the methyl radical, CH_3(X^2A_2''), has been measured to be $(2.1 \pm 1.3(-0.80)) \times 10^{-10}$ cm^3 molecule^{-1} s^{-1}, where the uncertainty includes both random and systematic errors at the 68% confidence level. The measurements were conducted over a pressure range of 2.8−4.3 Torr of CH_4 and at a temperature of 293 ± 2 K. The radicals were generated by the 248-nm photolysis of ClNCO in a large excess of CH_4. The subsequent rapid reaction, Cl + CH_4, generated the CH_3 radical. The rate constant for the Cl + CH_4 reaction was measured to be $(9.2 \pm 0.2) \times 10^{-14}$ cm^3 molecule^{-1} s^{-1}, where the uncertainty is the scatter of one standard deviation in the data. The progress of the reaction was followed by time-resolved infrared absorption spectroscopy on single rovibrational transitions from the ground vibrational level. Multiple species were detected in these experiments, including NCO, CH_3, HCl, C_2H_6, HCN, HNC, NH, and HNCO. Temporal concentration profiles of the observed species were simulated using a kinetic model, and rate constants were determined by minimizing the sum of the squares of the residuals between experimental observations and model calculations. Both HCN and HNC seem to be minor products (<0.3% each) of the NCO + CH_3 reaction. The peak concentrations of NH and HNCO were small, accounting for <1% of the initial NCO concentration; however, their temporal profiles could not be fit by the model kinetics. The observed C_2H_6 temporal profile always peaked at significantly higher concentrations than the model predictions, and several reaction models were constructed to help explain these observations. The most likely product channel seems to be the recombination channels, producing CH_3NCO and CH_3OCN.

I. Introduction

Radical−radical interactions are a unique class of chemical reactions that have important roles in many practical chemical problems such as combustion and atmospheric chemistry. The interaction of two species with unpaired electron spins leads to multiple spin manifolds and, if at least one of the species possesses electronic angular momentum, multiple electronic manifolds as well. The anti-pairing of electron spin can lead to bond formation without an activation barrier, so that recombination into a bound potential energy well corresponding to a chemical bond between the two radical fragments is at least one possible product channel. Another possibility is disproportionation of the two radicals, forming bimolecular products. Initially, the system possesses the energy of the newly forming bond and can have sufficient energy to be above potential energy barriers on the global potential energy surface (PES) that can lead to channels forming multiple products. Thus, radical−radical reactions can have the unique feature of multiple product channels. It is a significant theoretical challenge to predict the radical−radical rate constants for the recombination process accurately, because there is no obvious transition state along the reaction coordinate.[1]

The influence of multiple PESs on radical−radical reactions has always been an important issue in the description of radical−radical reactions.[2] Generally, only simple electronic degeneracy factors have been used; however, with the use of sophisticated theoretical techniques, the direct participation of excited PESs can be examined.[3] Twenty years ago, Smith[4] compared experimental recombination rate constant measurements to theoretical predictions for several simple radical−radical reactions and concluded that excited PESs made a significant contribution to the recombination process in many cases. In a recent work from this laboratory[5] on the NCO($X^2\Pi$) + Cl(^2P_u) reaction, it was suggested that intersystem crossing (ISC) was the reaction mechanism, producing triplet NCl($X^3\Sigma^-$) + CO($X^1\Sigma$) products, rather than recombination, forming singlet ClNCO(X^1A').

The NCO($X^2\Pi$) radical is an important combustion intermediate.[6] It is a major species that is involved in the production of NO_X compounds from two distinct combustion sources: the prompt or Fenimore mechanism and fuel-fixed nitrogen compounds.

The NCO radical also has an important role in the RaReNO$_x$ and NO$_x$OUT processes to remove NO$_x$ pollutants from flue gases. These treatments rely on the addition of cyanic acid ($(HONC)_3$) or urea ($(NH_2)_2CO$), respectively,[7] to the gas stream and the subsequent generation of NCO to remove NO. Despite these important roles that NCO has in combustion, there is sparse information available about its chemistry, especially its chemistry and kinetics with other transient species.

Another important radical in combustion chemistry is the CH_3(X^2A_2'') radical.[8] The combustion chemistry of hydrocarbon fuels ultimately degrades to the chemistry of C_1 carbon compounds, where the CH_3 radical is a major component. In addition, in the combustion of simple hydrocarbons, the CH_3

[†] Current address: Department of Chemistry, University of North Texas, P.O. Box 305070, Denton, TX 76203-5070.

* To whom correspondence should be addressed. Fax: (630) 252-9292. E-mail: rgmacdonald@anl.gov.

10.1021/jp058247b CCC: $33.50
Published on Web 12/21/2005

radical forms a building block leading to higher C_x compounds through self-recombination, forming C_2H_6 and subsequent radical addition reactions.

Radical−radical reactions pose an experimental challenge,[9] because, generally, the temporal dependence of the concentrations of two transient species must be followed. At the same time, the determination of product channel branching ratios requires that the concentrations of the products be measured.

In the current work, all these features of radical−radical reactions were applied to a study of the reaction

$$NCO(X^2\Pi) + CH_3(X^2A_2'') \xrightarrow{k_1} \text{products} \qquad (1)$$

The rate constant for reaction 1 (k_1) was measured, and possible products of the reaction were explored. The 248-nm photolysis of ClNCO and the rapid reaction of Cl atoms with a large excess of CH_4 created the initial NCO and CH_3 radical concentrations. Time-resolved infrared absorption spectroscopy was used to monitor the temporal concentration profiles of both NCO and CH_3, as well as six other species. As in previous work,[5,10,11] rate constants were determined by constructing a chemical model describing the system and varying the appropriate rate constants until the sum of squares of the residuals between the calculated and experimental temporal concentration profiles was minimized.

The formation of C_2H_6 was monitored in the experiment, so that the loss of CH_3 radicals from self-reaction could be directly taken into account in the model simulations. The reaction mechanism used to determine k_1 from analyzing the NCO temporal concentration profiles was not sufficient to explain all the experimental observations. As a result, the complete data set was analyzed using four other reaction models with slightly alternate reaction sequences. The influence of these altered reaction models on the determination of k_1 will be discussed.

Two isomers, CH_3NCO and CH_3OCN, can be formed in reaction 1 by direct recombination into bound adducts on a (X^1A') electronic PESs. These molecules are also found as potential minima on the global C_2-H_3-N-O PES, for which $C_2H_3(X^2A'') + NO(X^2\Pi)$ and $CH_3 + NCO$ are energetic asymptotes. There has been considerable interest[12−14] in the $C_2H_3 + NO$ system, because of its importance in reburn chemistry. The connections of the $NCO + CH_3$ energetic asymptote to the global C_2-H_3-N-O PES will be discussed.

A comparison of k_1 with theoretical predictions for the magnitude of the recombination rate constants forming CH_3NCO and CH_3OCN will be made. The theoretical rate constants were based on Troe's approximate statistical treatment[15] to estimate radical−radical high-pressure rate constants ($k_{rec,\infty}$). The direct recombination into the bound adducts on the singlet ground-state cannot explain the observed data, and the participation of excited electronic states seems necessary.

II. Experimental Section

The experimental apparatus has been described recently,[16] so only a brief description is given here. The stainless steel reaction chamber contained an inner Teflon box with dimensions of 100 cm × 100 cm × 5 cm. Two side chambers housed White cell optics, so that the infrared probe laser radiation could be multipassed through the volume of gas irradiated by the photolysis laser. The 248-nm photolysis and the probe laser beams were overlapped using an ultraviolet-infrared (UV−IR) dichroic mirror that was placed at Brewster's angle on the optical axis of the White cell. A ZnS plate, also at Brewster's angle, was placed in front of the opposite White cell mirror to absorb the transmitted UV radiation. This optic also deflected a small fraction of the photolysis laser beam out of the reaction chamber and onto a power meter, allowing the attenuation of the photolysis laser to be measured. The distance between these two optical elements defined the base optical path length of 139 cm. The optical path length was varied but was usually 16.2 m. The reaction chamber could be pumped out by a diffusion pump to a pressure of 5×10^{-6} Torr and had a leak rate of $\sim 5 \times 10^{-4}$ Torr/min.

The method of generating a constant flow of ClNCO and determining the concentration of ClNCO has been described.[5] The Ar and CH_4 gases were supplied by AGA and were 99.9995% and 99.99% pure, respectively. The gas flows were monitored by calibrated mass flowmeters. The flow rate of CH_4 varied between 300 sccm and 500 sccm, depending on the total pressure in the reaction chamber. The repetition rate of the photolysis laser was varied between 1 Hz and 3 Hz and was chosen so that a fresh sample of gas was irradiated on each laser pulse. The fluence of the photolysis laser at the input window of the reaction chamber was in the range of 5−25 mJ/cm^2. The attenuation of the photolysis laser through the apparatus was always <15% and generally <10%.

Continuous-wave infrared laser radiation was generated by a single-mode Burleigh model 20 color-center laser. This laser provides narrow line width (~1 MHz) radiation and is completely tunable from 2.65 μm to 3.38 μm, allowing for the detection of a variety of species. Each species except C_2H_6 was detected by isolated rovibrational transitions from the ground vibrational level. The largest source of noise in the experiments was amplitude fluctuations of the infrared laser, and various strategies for reducing these fluctuations have been described.[5]

Temporal absorption profiles of a probed species were recorded and signal-averaged, using a LeCroy Model 9410 digital oscilloscope. The initial probe laser intensity (I_0) was recorded using a boxcar that was triggered prior to the photolysis laser. Thermal lensing and refractive index changes in the optical elements exposed to the excimer laser resulted in oscillations superimposed on the absorption signal. These unwanted oscillations were removed by recording a background profile with the probe laser tuned to a region of zero absorption and subtracting the two traces. Data collection was controlled by a laboratory computer.

III. Results

A. Concentration Determination: NCO, CH_3, HCl, HCN, HNC, NH, and HNCO. Except for C_2H_6, all the species detected in the present work were monitored on single or near-degenerate transitions (NCO) involving isolated rovibrational transitions originating from the ground vibrational level. At thermal equilibrium, if the frequency (ν) is tuned to the maximum of an isolated absorption feature for species X, the absorbance ($A_X(\nu)$) is related to the concentration of X, [X], by

$$A_X(\nu) = \ln\left(\frac{I_0(\nu)}{I(\nu)}\right) = l\sigma_{pk}^X(\nu)[X] \qquad (E1)$$

where $I_0(\nu)$ and $I(\nu)$ are the initial and transmitted probe laser intensity at ν, respectively, l is the optical path length, and $\sigma_{pk}^X(\nu)$ is the peak absorption coefficient for the absorption feature.[17] The peak absorption coefficient is related to the length strength of the probed transition, $j \leftarrow i$, S_{ij}, by

$$\sigma_{pk}^X(\nu) = S_{ij}g_0(\nu) \qquad (E2)$$

TABLE 1: Spectroscopic Transitions and σ_{pk} for the Species Detected in This Work

molecule	upper level ← (0...)	wavelength (μm)	σ_{pk} (cm^2 molecule^{-1})	reference
NCO	(10^11) $P_{e/f}$(12.5)	3.165073	$(3.22 \pm 0.26) \times 10^{-19}$	5
NCO	(10^11) $P_{e/f}$(12.5)	3.165073	$(3.13 \pm 0.12) \times 10^{-19}$	this work
CH_3	ν_3 $^pP(3,3)$	3.196369	$(3.57 \pm 0.46) \times 10^{-18}$	18
HCl	v=1 $R^{37}(4)$	3.357090	$(2.02 \pm 0.02) \times 10^{-17}$	19
C_2H_6	ν_7 $^rQ_0$	3.348160	$(9.23 \pm 0.41) \times 10^{-18}$[a]	this work
C_2H_6	ν_7 $^pQ_3$	3.359333	$(6.71 \pm 0.37) \times 10^{-18}$[a]	this work
HCN	(001) P(8)	3.042058	$(3.90 \pm 0.15) \times 10^{-17}$	20
HNC	(100) R(10)	2.714005	$(1.10 \pm 0.05) \times 10^{-16}$[b]	21, 22
NH	v=1 $R_3(3)$	3.1098216	(3.89 ± 0.38) x 10^{-17}[c]	23, 24
HNCO	ν_1 $R_0(16)$	2.816516	$(5.2 \pm 0.05) \times 10^{-18}$	25

[a] Error estimate from the average scatter of all the measurements (see section III.B). Calculated at $P = 4.0$ Torr. [b] Calculated using a theoretical estimate of the HNC (100) transition dipole moment. The error estimate comes from experimental measurements (see ref 22). [c] Error estimate of 10% from difference in theoretically calculated transition moment (ref 24), and the experimental determination (ref 23). The experimental error estimate would be 26%; however, there is good agreement between theory and experiment.

where $g_0(\nu)$ is the peak of the normalized line shape function. At low pressures, $g_0(\nu)$ is related to the inverse of the Doppler width.

Except for a short induction period, for NCO,[5] CH_3,[18] HCl,[19] HCN,[20] HNC,[21,22] NH,[23,24] and HNCO,[25] equations E1 and E2 apply and known line strengths or measured peak absorption coefficients can be used to calculate the concentrations of these species, independent of pressure. Table 1 gives the most commonly used transitions and $\sigma_{pk}(\nu)$ for the species detected in the present experiments.

B. Concentration Determination: C_2H_6. The C_2H_6 molecule was detected using several spectral features of the ν_7 C−H stretching fundamental vibrational band at ~2990 cm^{-1}. A unique feature of the ν_7 transition is the presence of extremely sharp Q sub-branches that result from the overlap of all the J transitions in each of the $^rQ_4$ to $^pQ_4$ sub-bands. The formation of these large absorption features provides a sensitive means for detecting a relatively large polyatomic molecule by infrared absorption spectroscopy. These spectral features are further complicated by torsional tunneling and A_1-A_2 splittings, making a simple spectral simulation difficult.[26] Thus, it was decided to determine the maximum absorption coefficient for several of these Q sub-bands features experimentally, under the conditions of the experiment.

The measurements were performed in the reaction chamber with the White cell optics removed and a single pass of the infrared laser radiation. The $^rQ_0$ and $^pQ_3$ sub-branches were selected for investigation, because their detailed structure has been analyzed.[26] The measurements were performed at C_2H_6 pressures ($P_{C_2H_6}$) in the range of 0.006−0.051 Torr, with the remaining gas being CH_4, as in the rate constant determination experiments. Thus, any gas-specific pressure broadening effects were directly included in the measurements. Under these conditions, the absorbance varied from ~0.3 to 2.5.

The gas mixtures were either composed in large storage bulbs and allowed to mix for several days before use or prepared directly in a flow cell arrangement. Within the scatter of the data, the determination of $\sigma_{pk}^{C_2H_6}$ was independent of the method of sample preparation.

A typical scan over the C_2H_6 ν_7 $^rQ_0$ sub-branch is shown in Figure 1a. The results of the measurements for the $\sigma_{pk}(\nu)$ for the most prominent absorption feature in Figure 1a are shown in Figure 1b, as a function of CH_4 pressure. Figure 2 shows similar results for the $^pQ_3$ sub-branch. For both transitions, the

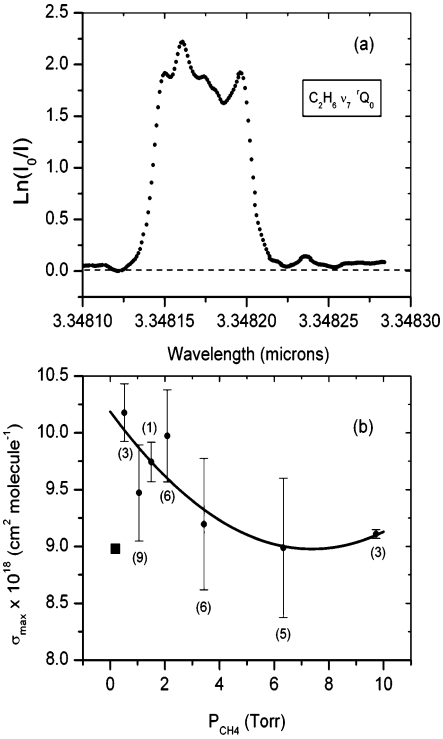

Figure 1. (a) Typical absorption scan over the C_2H_6 ν_7 $^rQ_0$ sub-branch spectral region; the experimental conditions were $P_{CH_4} = 3.219$ Torr and $P_{C_2H_6} = 0.0509$ Torr at a temperature of $T = 293$ K. (b). Summary of the experimental measurements for the maximum absorption coefficient as a function of P_{CH_4}. (In panel b, the numbers given in parentheses are the number of determinations at that P_{CH_4} value. The error bars are one standard deviation ($\pm 1\sigma$) in the scatter in the measurements. The solid square (■) symbol is an estimate of the maximum absorption coefficient from Figure 1 of ref 26 at a total pressure of $P_{C_2H_6} = 0.190$ Torr and $T = 296$ K.)

decrease in $\sigma_{pk}(\nu)$ with increasing pressure seems to be real and indicates the subtle effects pressure broadening can have on these transitions. The square points in Figures 1b and 2b are calculated absorption coefficients, using data from several figures from the work of Pine and Stone.[26] The value of $\sigma_{pk}(\nu)$ for both transitions at a pressure of 4.0 Torr is given in Table 1.

C. Reaction Mechanism. The detail reaction mechanism describing the reactions considered in the NCO−CH_3 reaction scheme[27−35] is given in Table 2, and the enthalpies[36−43] of formation ($\Delta H_{f,0}^0$) for the species in the reaction mechanism are summarized in Table 3. The five most important chemical reactions in the system are reactions 1, 2, 3, 7, and 11.

The kinetic equations describing the reaction mechanism were integrated using a fourth-order Runge−Kutta procedure[44] to give temporal concentration profiles of each species. The least-squares minimization procedure for the determination of optimized rate constants has been described.[5] Also included in the optimization procedure was an estimate of the 68% confidence limits on the determined rate constant.

To visualize how well a particular computer-generated concentration profile fit the experiment, a χ^2 related function, $\overline{\chi_N^2}(X)$, was defined as

$$\overline{\chi_N^2}(X) = \sum_{i=1} \frac{(1 - [X]_i^{Mod}/[X]_i^{Exp})^2}{N_{pts}} \qquad \text{(E3)}$$

where i is the data point number for time t, N_{pts} the total number of data points, $[X]_i^{Mod}$ is the calculated concentration and

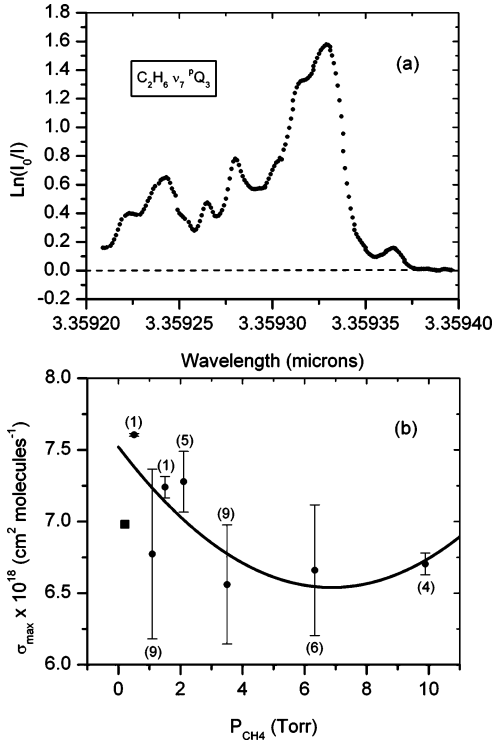

Figure 2. (a) Typical absorption scan over the C_2H_6 ν_7 $^PQ_3$ sub-branch spectral region; the experimental conditions were $P_{CH_4} = 6.159$ Torr and $P_{C_2H_6} = 0.0478$ Torr. (b) Summary of the experimental measurements for the maximum absorption coefficient as a function of P_{CH_4}. (In panel b, the numbers given in parentheses are the number of determinations at that P_{CH_4} value. The error bars are one standard deviation ($\pm 1\sigma$) in the scatter in the measurements. The solid square (■) symbol is an estimate of the maximum absorption coefficient from Figure 2 of ref 26 at a total pressure of $P_{C_2H_6} = 0.210$ Torr and a temperature of 296 K.)

$[X]_i^{Exp}$ is the observed concentration, respectively, of X at point *i*. The square root of $\overline{\chi^2_N}(X)$ was used to calculate the average fraction between the calculated and experimental profiles, $\overline{[X]}_{Mod}/\overline{[X]}_{Exp}$. If the average fraction is zero the overlap is perfect, and if the average fraction is 1 or 0.25, the calculated profile is, on average, a factor of 2 greater or smaller than the experimental profile. The appropriate situation can be determined from the average deviation for the profile.

In the present experiment, the only source of HCl was reaction 2 and the only significant loss of Cl atoms was reaction 3. Thus, the HCl concentration profile can be used to determine the initial radical concentration and provide a new measurement of σ_{pk}^{NCO}. The initial NCO, equal to the Cl concentration, was varied until the maximum in the calculated HCl concentration agreed with the observed value to within ±0.5%. This provided the initial radicals concentrations for subsequent rate constant optimization. The initial absorbance of NCO was determined by extrapolating the first 50 μs of the NCO absorbance profile back to $t = 0$. Polyatomic collision partners such as CH_4 are more efficient at vibrationally relaxing NCO than inert gases such as argon,[45,46] so that any induction period due to vibrational relaxation will be shorter in CH_4 than in argon. Equation E1 can be used to calculate σ_{pk}^{NCO}, using the known path length. The new measurement of σ_{pk}^{NCO} was determined to be $(3.13 \pm 0.12) \times 10^{-19}$ cm^2/molecule and is included in Table 1.

The only rate constant in the basic reaction mechanism outlined in Table 2 that has not been previously measured is reaction 1. In preliminary investigations of the appropriate reactions to include in the basic reaction mechanism, reaction 12 (CH_3 + ClNCO) was considered; however, no evidence was observed to indicate that this reaction was important. It was included in the final mechanism, for completeness.

D. Diffusional Loss. Diffusion is an important loss process in the reaction scheme, particularly for NCO and CH_3 at long times. The first-order rate constant for diffusional loss for species X, k_{Diff}^X, diffusing in species B is the product of a binary diffusion constant, D_{XB}, and a geometrical factor describing the boundary conditions of the experiment. The D_{XB} were calculated using the method developed by Fuller et al.[47,48] based on specially derived atomic diffusion volumes, υ_k (given in units of cm^3) and is given by

$$D_{XB}(\mathrm{cm}^2/\mathrm{s}) = \frac{0.760T^{1.75}}{P\sqrt{\mu}[(\sum_X \upsilon_k^{1/3}) + (\sum_B \upsilon_k^{1/3})]^2} \qquad \text{(E4)}$$

where T is the temperature (in Kelvin), P the pressure (in Torr),

TABLE 2: Summary of the Reactions and Rate Constants Used To Model the NCO + CH_3 System for 293 K[a]

number	reactants		products	k (cm^3 molecule^{-1} s^{-1})[b]	reference(s)
1a	NCO +CH_3	→	CH_3NCO	optimized	see text
1b		→	HCN + H_2CO	optimized	
1c		→	HNC + H_2CO	optimized	
1d		→	*$CH_3N(X^3A_2") + CO$*	*fixed*	see text
2	Cl + CH_4	→	CH_3 + HCl	$(9.7 \pm 0.1) \times 10^{-14}$	27, 28
3	Cl + NCO	→	NCl($X^3\Sigma^-$) + CO	$(6.9 \pm 3.8) \times 10^{-11}$	5
4	Cl + ClNCO	→	NCO + Cl_2	$(2.4 \pm 1.6) \times 10^{-13}$	5
5	Cl + CH_3	→	CH_3Cl	2.0×10^{-11}	29
6	Cl + C_2H_6	→	C_2H_5 + HCl	$(5.5 \pm 0.2) \times 10^{-11}$	30
7	NCO + NCO	→	N_2+ 2CO	$(5.0 \pm 2.0) \times 10^{-12}$	31
8	NCO + CH_4	→	CH_3 + HNCO	2.0×10^{-16}	32
9	NCO + C_2H_6	→	C_2H_5 + HNCO	$(2.0 \pm 0.4) \times 10^{-14}$	33
10	*NCO + CH_3NCO*	→	*$CH_3 + N_2 + 2CO$*	*fixed*	see text
11	CH_3 + CH_3	[CH_4]	C_2H_6	$(5.0 \pm 0.2) \times 10^{-11}$	34
11	*CH_3 + CH_3*	→	*C_2H_6*	*optimized*	see text
12	CH_3+ ClNCO	→	CH_3Cl + NCO	1.0×10^{-16}	fixed
13	*CH_3 + CH_3NCO*	→	*C_2H_6+ NCO*	*optimized*	see text
14	NCl + NCl	→	Cl_2 + N_2	$(8.1 \pm 1.8) \times 10^{-12}$	35
15	*CH_3N + CH_3N*	→	*$C_2H_6 + N_2$*	*optimized*	see text
16	X	k_{diff}^X →	X	Eq. E5	see text

[a] Reactions in italics were included in separate model scenarios, to probe the observation that reaction 11 alone could not explain the excess [C_2H_6] observed. [b] All rate constants are given as effective second-order rate constants.

TABLE 3: Summary of the $\Delta H^0_{f,0}$(X) of the Species in the NCO + CH_3 Reaction Models

species	$\Delta H^0_{f,0}$(X) (kJ/mol)	reference
NCO($X^2\Pi$)	128 ± 0.8	36
Cl(^2P_u)	119.62 ± 0.008	37
CH_3(X^2A_2'')	150.0 ± 0.3	37
NH($X^3\Sigma^-$)	359.5 ± 0.3	38
NCl($X^3\Sigma^-$)	325 ± 5	39
C_2H_5(X^2A'')	132 ± 2.4	40
CH_4	−66.63 ± 0.3	37
ClNCO	53[a] ± 30[b]	this work
HCl	−91.992 ± 0.006	41
C_2H_6	−68.4 ± 0.3	42
HCN	132 ± 4	42
HNC	193 ± 4	42
HNCO	−115.5 ± 0.8	36
CH_3NCO	−78[a] ± 30[b]	this work
CO	−113.81 ± 0.17	37
H_2CO	−104.9 ± 0.5	37
CH_3Cl	−73.9 ± 0.7	42
CH_3N(X^3A_2'')	368	43

[a] This work. DFT-B3LYP/6-311++G** calculations with ZPE corrections using an empirical factor of 0.92 for the vibrational frequencies. [b] Estimate of uncertainty.

and μ the molar reduced mass between X and B. The k^X_{Diff} values were determined by normalizing calculated D_{XB} values to the experimentally measured value for k^{HCl}_{Diff}. The k^X_{Diff} values for HCl, C_2H_6, HCN, and HNC were determined experimentally, and the agreement between the calculated and experimental values of k^X_{Diff} for C_2H_6, HCN, and HNC was ~10%, similar to the scatter in the measurements.

E. Using the Basic Reaction Mechanism To Determine k_1. Figures 3−5 show the species concentration temporal profiles for an experiment conducted at a partial pressure of CH_4 (P_{CH_4}) of 3.78 Torr. In each figure, the points are the experimental determination of the indicated species concentration, and the lines, straight and dashed, are simulations, using the basic kinetic mechanism presented in Table 2. The reactions in the basic mechanism are listed in normal type in Table 2 and are identified as reactions 1a, 1b, 1c, 2, 3, 4, 5, 6, 7, 8, 9, 11, 12, and 14, plus the diffusion of each species. The reactions given in italics were added to the basic mechanism in several different scenarios that will be discussed in section III.F.

Figure 3 shows the agreement between the model predictions and the experimental NCO and CH_3 concentration profiles. As is evident from the figure, for the NCO species, the agreement between the model calculations and experiment is excellent. A summary of the experimental conditions and results for the determination of k_1 is given in Table 4. Using the basic mechanism, the average value of k_1 was determined to be (2.1 ± 0.4) × 10^{-10} cm^3 $molecule^{-1}$ s^{-1}, where the scatter is one standard deviation from the mean (±1σ). The measurements were performed at a temperature of 293 ± 2 K. The determination of k_1 using the basic mechanism is also shown as a function of the initial NCO concentration ([NCO]$_0$) in Figure 6a. The error bars in the figure are the 68% confidence level in the goodness of fit.

The long dashed line in Figure 3 gives the model prediction for the CH_3 profile. The agreement between the model predictions and experiment is not as good for CH_3 as for NCO. Although both the model and experimental CH_3 profiles reach their maximum at similar times, the model predicts a maximum CH_3 concentration that is 25% greater than the experiment. Similar behavior was observed for all the experimental runs. For all the experiments, the average value of the peak $[CH_3]_{exp}/[CH_3]_{model}$ was 0.87 ± 0.07, where the uncertainty is ±1σ. Part

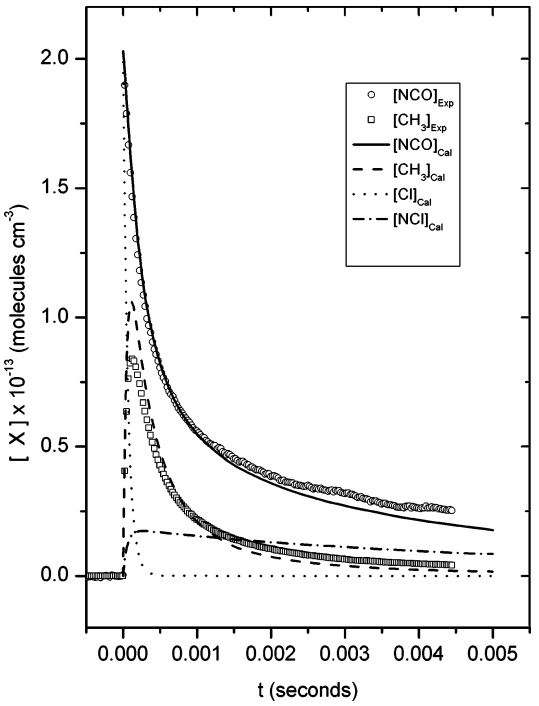

Figure 3. Typical experimental temporal concentration profiles for (○) NCO and (□) CH_3 are compared to the predictions of the basic reaction model summarized in Table 2. The optimum value of k_1 was determined using the NCO profile, and was determined to be (1.7 ± 0.4) × 10^{-10} cm^3 $molecule^{-1}$ s^{-1}. For clarity, the experimental data points are shown for every 10th data point. Calculated concentration profiles are also plotted: (—) NCO, (− − −) CH_3, (• • •) Cl, and (− • −) NCl. The conditions of the experiment were P_{Ar} = 0.26, P_{CH_4} = 3.77, and P_{ClNCO} = 0.011 Torr at 293 ± 1 K.

of the discrepancy between the model predictions and experiment for the CH_3 profiles could be resolved using a correspondingly smaller $\sigma^{CH_3}_{pk}$. As indicated in Table 1, $\sigma^{CH_3}_{pk}$ is the absorption coefficient with the largest uncertainty; however, scaling the experimental profile to match the model predictions generally resulted in poorer agreement in the decaying portions of the CH_3 profiles.

Figure 4a shows the production of HCl from reaction 2. The model prediction for the HCl profile, using the average of two recent literature recommendations[27,28] for k_2—(9.7 ± 0.1) × 10^{-14} cm^3 $molecule^{-1}$ s^{-1} at 293 K—is shown by the long dashed line. The solid line in the figure is the determination of an optimized value for k_2. The results of these measurements are summarized in Table 4. The value of k_2 was determined to be (9.2 ± 0.2) × 10^{-14} cm^3 $molecule^{-1}$ s^{-1}, where the uncertainty is ±1σ. There is good agreement between the measured and accepted value of k_2, indicating there was no other significant secondary source of HCl.

Figure 4b shows the production of C_2H_6 in the same experiment. The only source of C_2H_6 is the recombination of CH_3 radicals (reaction 11). The negative population excursion over the first 100 μs indicates that a significant population inversion occurred between the ground state and $\nu_7 = 1$. Another feature of Figure 4b is the underprediction for the formation of C_2H_6 using the established rate constant for k_{11}.[34] Similar behavior was observed for all the experimental runs. The average value for the ratio of the maximum values for $[C_2H_6]_{exp}/[C_2H_6]_{mod}$ was 1.38 ± 0.14.

There are several possibilities that could explain this discrepancy. The first is the uncertainty in the absorption coefficient measurements for C_2H_6. The results for this measurement are summarized in Figures 1b and 2b. The mean experimental

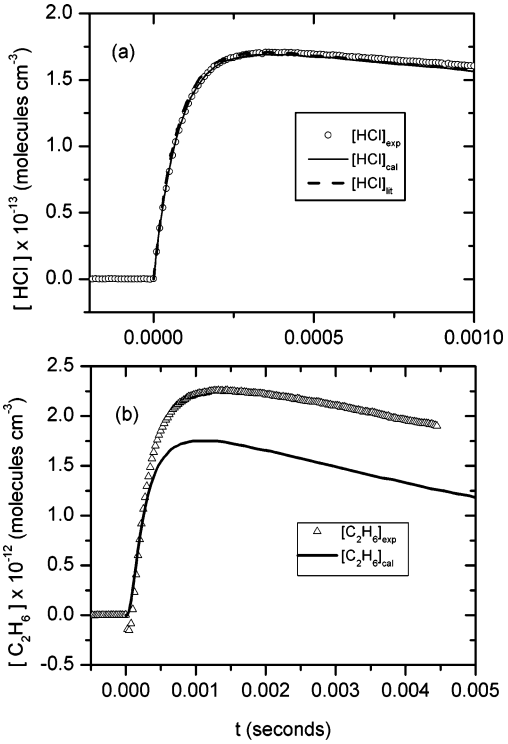

Figure 4. (a) HCl experimental concentration profile obtained in the same experiment as that shown in Figure 3; the experimental points (○) are shown every 10th data point; the solid line (—) is the calculated HCl concentration profile using an optimized determination of k_2, and it was determined to be $(9.1 \pm 1.6) \times 10^{-14}$ cm^3 molecule^{-1} s^{-1}; the dashed line (– – –) slightly above the solid line is the HCl concentration profile using the evaluated k_2 in Table 2. (b) C_2H_6 experimental concentration profile; the experimental data points (Δ) are shown every 10th data point, and the solid line (—) is the prediction of the C_2H_6 concentration profile using the recombination rate constant recommended by Slagle et al.[34] for k_{11}. At the pressure of the experiment, the value of k_{11}, as a second-order rate constant, was 4.9×10^{-11} cm^3 molecule^{-1} s^{-1}. Note the population inversion indicated by the negative population transient at the beginning of the C_2H_6 profile.

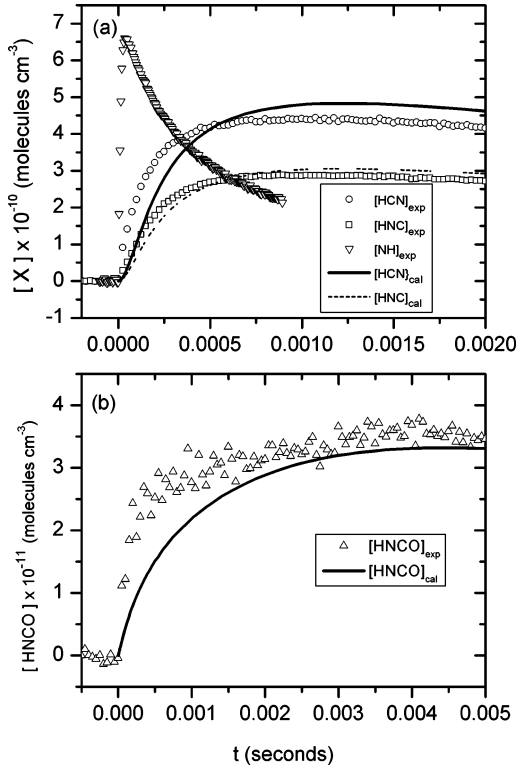

Figure 5. (a) The experimental profiles for (∇) NH, (○) HCN, and (□) HNC, obtained in the same experimental run as Figure 3. As discussed in the text, NH is believed to be from N(^{2}D) + CH_4. The solid line (—) is the optimum value of $k_{1b} = (8.6 \pm 1.4) \times 10^{-13}$ cm^3 molecule^{-1} s^{-1}, and the dashed line (- - -) is the optimum value of $k_{1c} = (5.0 \pm 0.5) \times 10^{-13}$ cm^3 molecule^{-1} s^{-1}, both obtained using the basic reaction mechanism in Table 2. The data points are shown every 10th point. (b) Experimental profile for (Δ) HNCO; the solid line (—) is the calculation of the HNCO concentration profile for k_8 adjusted to be 2.0×10^{-16} cm^3 molecule^{-1} s^{-1}. Again, the data points are shown every 10th point.

scatter in the C_2H_6 absorption coefficient measurements was approximately ±4%; thus, experimental uncertainty cannot explain the underprediction of the C_2H_6 concentration. A second possibility is an underlying absorption signal from a product of reaction 1, either CH_3NCO and/or CH_3OCN, or an unknown stable species produced in the system. Indeed, both CH_3NCO[49] and CH_3OCN[50] have known C−H stretching absorptions in the υ_7 C−H stretching spectral region of C_2H_6. There are no high-resolution spectra available for vibrational transitions of these CH_3NCO isomers; however, at low resolution, there are prominent Q branch features centered at 3.391 and 3.369 μm, respectively. No attempts were made to detect these Q branch features. The Q branch feature of the C−H asymmetric CH_3NCO vibration is just beyond the practical operating range of the color center laser, and the possibility of the CH_3OCN product channel was not appreciated until the experiments were completed. However, the possibility of interfering absorptions in the C_2H_6 spectral region was considered. This was the motivation for monitoring C_2H_6 on two separate transitions, $^rQ_0$ and $^pQ_3$. These are shifted 20 and 10 cm^{-1} to the high-frequency side of the CH_3OCN Q branch feature, respectively. It is unlikely that unknown absorptions interfered with the monitoring of the C_2H_6 concentration. No detectable difference, within experimental scatter, was observed in monitoring C_2H_6 using either transition. The Q-branch region of the weaker C−H symmetric vibration is reported[49] to be ∼3.300 cm^{-1}. The probe laser was also manually scanned throughout the 3.30−3.36 μm region. No transitions could be observed that were not due to either ground or excited vibrations of CH_4. The third and most likely possibility is that C_2H_6 was being produced in a reaction that was not taken into account in the basic mechanism. This prompted an investigation into the possibility that other reactions should be added to the basic reaction mechanism, and this will be discussed in section III.F.

Figure 5a shows the experimental temporal concentration profiles for HCN, HNC, and NH. Although the signal-to-noise ratio for all three species is good after signal averaging, there is some uncertainty in tuning the probe laser to the peak of these transitions, because of small single-shot absorption signals. As is evident from Figure 5a, the experimental appearances of HCN and HNC are faster than the model predictions for the optimum values of k_{1b} and k_{1c}. This was characteristic for all the HCN and HNC profiles recorded. There is no clear explanation of the apparent rapid appearance of HCN or HNC. Depending on the extent of vibrational excitation in reactions 1b and 1c and the rate of vibrational relaxation into the ground state, the apparent appearance rate of the HCN or HNC could be greater than the reaction rate. CH_4 has been observed to relax excited stretch and bend stretch vibrational levels of HCN efficiently;[51,52] however, there is no information about the relaxation of the less-energetic pure bending levels. In any case, if HCN and HNC are indeed products of reaction 1, channels 1b and 1c account for <0.6% of the products. The results of these measurements are summarized in the fifth and sixth

TABLE 4: Summary of the Rate Constant Measurements Determined Using the Basic Reaction Mechanism

Partial Pressure (Torr)		$[NCO]_0$	Rate Constants (cm^3 $molecule^{-1}$ s^{-1})			
P_{CH_4}	P_{ClNCO}	($\times 10^{13}$ molecule/cm^3)	k_1[b] ($\times 10^{-10}$)	k_{1b} ($\times 10^{-13}$)	k_{1c} ($\times 10^{-13}$)	k_2 ($\times 10^{-14}$)
4.33	0.011	2.49	1.7 ± 0.3[a]	6.7 ± 1.8	3.2 ± 0.4	9.2 ± 0.4
4.33	0.0073	1.71	2.4 ± 0.4	15 ± 4.0	5.8 ± 0.6	9.2 ± 0.3
4.33	0.0076	1.69	2.3 ± 0.3			
4.39	0.032	3.09	2.3 ± 0.2	$4.6 \pm 0.0.7$	3.9 ± 0.4	8.7 ± 1.7
3.78	0.0074	0.818	1.4 ± 0.3			9.0 ± 1.0
3.78	0.012	2.02	1.7 ± 0.3	8.6 ± 1.4	5.0 ± 0.5	9.1 ± 1.6
3.17	0.0040	0.830	2.3 ± 0.8			9.3 ± 0.2
3.17	0.0055	0.734	2.0 ± 0.2			9.2 ± 0.4
3.18	0.013	2.33	2.1 ± 0.4	8.8 ± 1.2	5.5 ± 0.6	9.6 ± 1.6
2.85	0.015	2.49	2.2 ± 0.8	5.0 ± 0.5	4.1 ± 0.2	9.1 ± 0.6
2.83	0.016	1.46	1.6 ± 0.2	7.4 ± 1.5	6.1 ± 0.6	9.1 ± 0.4
4.48	0.028	3.14	2.3 ± 0.8			9.3 ± 0.1
4.48	0.025	2.88	2.0 ± 0.7			9.3 ± 0.2
3.20	0.0083	2.40	2.6 ± 0.7	9.0 ± 2.0		9.2 ± 0.8
3.20	0.0083	1.55	2.71 ± 0.7			9.5 ± 0.6
summary			2.1 ± 0.4[b]	8.1 ± 3.6	4.7 ± 1.0	9.2 ± 0.2

[a] The uncertainties represent the 68% confidence limit in the optimized rate constant. [b] The uncertainties in the average rate constants are $\pm 1\sigma$.

columns in Table 4, with $k_{1b} = (8.1 \pm 3.6) \times 10^{-13}$ and $k_{1c} = (4.7 \pm 1.0) \times 10^{-13}$ cm^3 $molecule^{-1}$ s^{-1}, where the uncertainties are $\pm 1\sigma$. Reaction 1b accounts for (0.39 ± 0.24)% of the products from reaction 1 and reaction 1c accounts for (0.22 ± 0.09)% of the products.

Also included in Figure 5b is an experimental profile for the NH radical. No reaction sequence could be devised that explained the time characteristics of the NH radical if it were a product of reaction 1. However, Bell and Coombe[53] reported the production of electronically excited N(^{2}D) atoms from multiple photon absorption in ClNCO at 248 nm, so that a likely source of NH is the reaction of N(^{2}D) + CH_4. Theoretical calculations[54] indicate the two main product channels for the reaction of N(^{2}D) with CH_4 are CH_3N + H and NH + CH_3; however, the actual branching fraction is dependent sensitively on the PES that describes the reaction.

The appearance rate of NH was measured in six experiments, in which P_{CH_4} varied over a range of 2.87−4.35 Torr. Treating the appearance rate of NH as due to the N(^{2}D) + $CH_4 \rightarrow CH_3$ + NH reaction, an estimate of the rate constant for this reaction was $(9.7 \pm 1.4) \times 10^{-13}$ cm^3 $molecule^{-1}$ s^{-1}. The total loss rate for the N(^{2}D) + CH_4 reaction has been reported[55] to be 5.6×10^{-12} cm^3 $molecule^{-1}$ s^{-1}. Assuming that electronic quenching is small, these measurements can be used to provide an estimate for the branching ratio into the NH + CH_3 channel to be 0.18. As shown in Figure 5a, the observed concentration of NH was small ($<1.0 \times 10^{11}$ molecules/cm^3). The average yield of N(^{2}D) from the sequential photolysis of ClNCO, compared to the NCO radical, was (0.36 ± 0.3)%; thus, the generation of NH was small enough to be safely ignored in the data analysis.

Figure 5b shows the temporal profile for HNCO. The figure clearly shows that the signal-to-noise ratio is not as good for HNCO as it is for the other species. This is characteristic of operating the color-center laser in the 2.85-μm wavelength range. The solid curve is the model calculation with $k_8 = 2.0 \times 10^{-16}$ cm^3 $molecule^{-1}$ s^{-1}. A previous study[32] had set an upper limit of 1.0×10^{-14} cm^3 $molecule^{-1}$ s^{-1} for k_8 at 295 K. Although the signal-to-noise ratio is poor, the rise in the HNCO profile seems to be faster than if reaction 8 were the generating reaction. Only a few profiles of HNCO were collected, because of the time needed to align the probe laser cavity to operate in the HNCO wavelength region and the low yield of HNCO. In any case, it is likely k_8 cannot be larger than 2.0×10^{-16} cm^3 $molecule^{-1}$ s^{-1}, which is a substantially lower estimate than the previously available value near 295 K.

F. Modified Reaction Mechanisms. The basic reaction mechanism (Table 2) was modified by adding different reaction scenarios. These modified mechanisms explored the types of reactions that could bring about better agreement between model and experimental predictions for the C_2H_6 and CH_3 concentration profiles, and they explored the influence that different reaction models could have on the determination of k_1. Four different mechanisms were investigated, and they will be discussed in terms of the experimental data in Figures 3−5. All the experimental runs were analyzed using each reaction mechanism.

F(i). Variable Rate Constants k_1 and k_{11}. The most noticeable disagreement between the model predictions and experiment involved the C_2H_6 concentration profiles. The value of k_{11} used in the basic model was taken as the value of k_{11} with argon as a bath gas. At a pressure of 4.0 Torr Ar, k_{11} is within 75% of its high-pressure limit, $k_{rec\infty}$, which was determined to be 6.3×10^{-11} cm^3 $molecule^{-1}$ s^{-1} in a recent theoretical calculation.[3] If CH_4 is a significantly more-efficient energy transfer partner than argon, the system could be closer to the high-pressure limit. To investigate this possibility, k_{11} was treated as a variable rate constant in model F(i). However, because the variation in k_{11} changed the CH_3 concentration, k_1 was also optimized. The results are shown in Figure 7a for the NCO concentration profile and in Figure 7b for the C_2H_6 profile. As is evident from comparing Figures 4b and 7b, there is a modest improvement in the model predictions for the C_2H_6 profile, the average fraction $[C_2H_6]_{mod}/[C_2H_6]_{exp}$ changes from 0.75 in Figure 4b to 1.19 in 7b. For this experiment, the optimized value of k_{11} was determined to be $(9.0 \pm 2.0) \times 10^{-11}$ cm^3 $molecule^{-1}$ $s,^{-1}$ almost 43% larger than the accepted high-pressure limit rate constant for reaction 11, and k_1 increased to $(2.1 \pm 0.25) \times 10^{-10}$ cm^3 $molecule^{-1}$ s^{-1}.

A summary of the complete analysis of the data using this model (referenced hereafter as F(i)) is provided in Figure 6b with the optimized rate constants k_1 and k_{11} plotted as a function of the initial NCO radical concentration. The general trends that appeared in the analysis of the single experiment shown in Figures 3−5 applied to the complete data set. Using reaction mechanism F(i), the average value of k_1 increased to $(2.7 \pm 0.7) \times 10^{-10}$ cm^3 $molecule^{-1}$ s^{-1} and the average value of k_{11} was $(1.0 \pm 0.3) \times 10^{-10}$ cm^3 $molecule^{-1}$ s^{-1}. For model F(i) to account for the observed concentration of C_2H_6, the high-

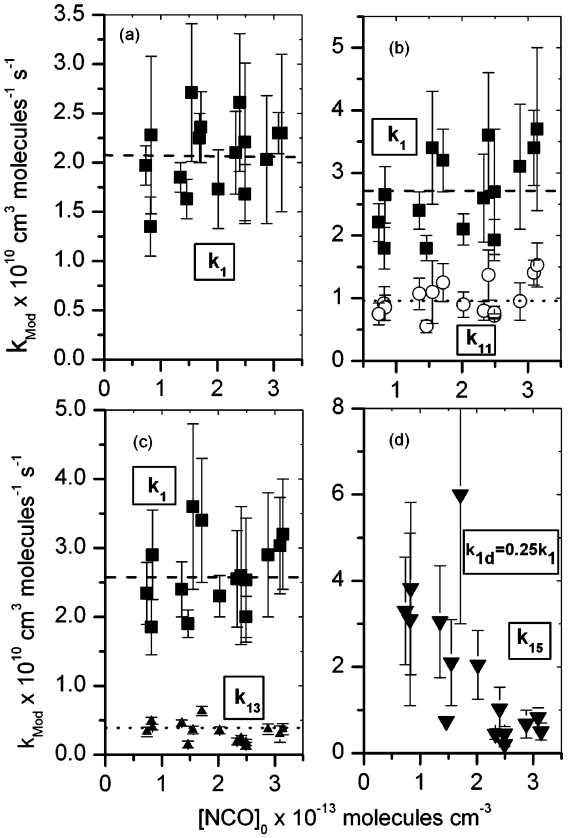

Figure 6. Summary of the data analysis using different kinetic models to determine k_1 as a function of $[NCO]_0$. Panel a shows k_1 values determined using the basic mechanism given in Table 2 ((■) k_1 values determined using the basic mechanism, and (- - -) average k_1 value, $k_1 = (2.1 \pm 0.4) \times 10^{-10}$ cm^3 molecule^{-1} s^{-1}). Panel b shows the results for (■) k_1 and (○) k_{11}, using mechanism F(i). Both k_1 and k_{11} were optimized. The dashed lines are the average values, $k_1 = (2.7 \pm 0.7) \times 10^{-10}$ cm^3 molecule^{-1} s^{-1} and $k_{11} = (1.0 \pm 0.3) \times 10^{-10}$ cm^3 molecule^{-1} s^{-1}. Panel c shows the results for (■) k_1 and (▲) k_{13}, using mechanism F(ii) as discussed in the text. The dashed lines are the average values, ($k_1 = 2.6 \pm 0.5$) $\times 10^{-10}$ and $k_{13} = (3.3 \pm 1.4) \times 10^{-11}$ cm^3 molecule^{-1} s^{-1}. Panel d shows the results for (▼) k_{15}, using mechanism F(iv) as discussed in the text. The best fits were obtained with $k_{1d} = 0.25k_1$. The large variation with $[NCO]_0$ indicates that this model is not acceptable.

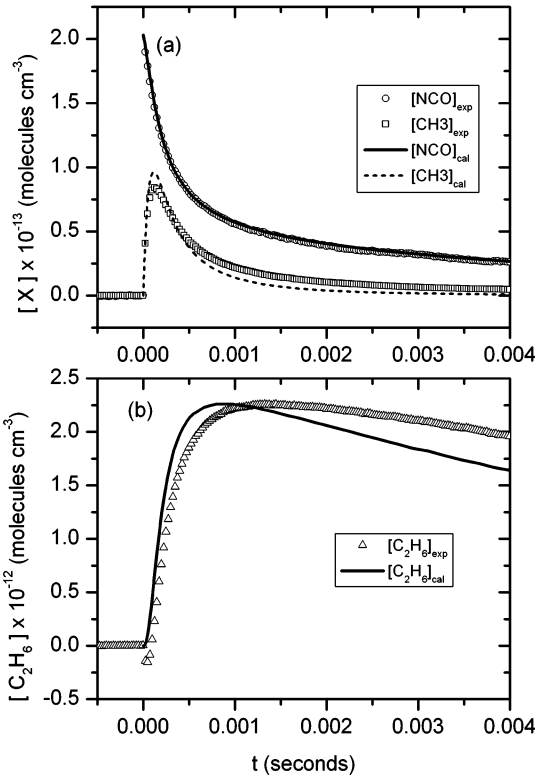

Figure 7. (a). Model F(i) to fit the C_2H_6 concentration profile by varying k_{11}. Both k_1 and k_{11} were iteratively optimized. The experimental curves for (○) NCO and (□) CH_3 are the same as in Figure 3a. The solid line (—) is the modified model calculation for NCO optimizing k_1 to fit the NCO profile. The value of k_1 was determined to be (2.1 ± 0.25) $\times 10^{-10}$ cm^3 molecule^{-1} s^{-1} for the optimum value of k_{11} (see Figure 7b). (b) Same experimental C_2H_6 profile (data points represented by open triangles (Δ)) as in Figure 4b, and the model predictions for the C_2H_6 profile using optimum values of both k_1 and k_{11}. The optimized value of k_{11}, expressed as a second-order rate constant, was determined to be (9.0 ± 2.0) $\times 10^{-11}$ cm^3 molecule^{-1} s^{-1}, almost a factor of 2 greater than the accepted value of k_{11} at this pressure.

pressure limit of k_{11} would have to be almost 1.0×10^{-10} cm^3 molecule^{-1} s^{-1}. This is 1.6 times larger than the currently accepted value at 300 K, which is too large a deviation from the accepted value. Some other chemistry must contribute to C_2H_6 production.

F(ii). Variable Rate Constants k_1 and k_{13}. Although vibrational relaxation of C_2H_6 complicates the interpretation of the initial portion of the C_2H_6 concentration profiles, the C_2H_6 concentration profiles calculated using model F(i) clearly rose too quickly and peaked earlier than the experimental profile. The requirement to fit both the NCO and C_2H_6 concentration profiles severely restricts the range of acceptable rate constants for k_1 and k_{11}. The model described in this subsection (hereafter referenced as F(ii)) consisted of the reactions in the basic mechanism with the addition of reaction 13. Reaction 13 was added to the basic mechanism because it removes CH_3 and produces C_2H_6. Using the $\Delta H^0_{f,0}$ values listed in Table 3, reaction 13 is predicted to be −12 kJ/mol exothermic and might be expected to be slow. A more likely candidate might be the more-exothermic reaction $CH_3 + CH_3OCN$; however, because of the considerable uncertainty in the $\Delta H^0_{f,0}$ and the unknown branching ratio between these two channels, only reaction 13 was considered. In any case, it is perhaps better to view reaction 13 as a reaction of CH_3 with a product of reaction 1 leading to C_2H_6 in order to better determine the parametrization of the rate constants needed to fit the NCO, CH_3, and C_2H_6 profiles.

Both k_1 and k_{13} were iteratively optimized to obtain the best agreement between the model predictions and the experimental concentration profiles for NCO and C_2H_6, respectively. The results are shown in Figure 8 for the experimental run illustrated in Figures 3 and 4. For this experiment, the optimized values of k_1 and k_{13} were determined to be (2.3 ± 0.3) $\times 10^{-10}$ and (3.5 ± 0.5) $\times 10^{-11}$ cm^3 molecule^{-1} s^{-1}, respectively. As is evident from comparing figures 4b and 8b, the model F(ii) prediction of the C_2H_6 profile is in much better agreement with the experiment than the basic mechanism. The average fraction $\overline{[C_2H_6]_{mod}/[C_2H_6]_{exp}}$ has increased to 0.95. Comparing Figures 8a and 3, the model F(ii) predictions for the NCO and CH_3 profiles are similar for NCO but actually slightly worse for CH_3.

A summary of the determination of k_1 and k_{13} obtained using model F(ii) is shown in Figure 6c, again by plotting k_1 and k_{13} as a function of the initial NCO concentration. Although there is some scatter in the results, the fact that there is no apparent dependence of k_1 or k_{13} on radical concentration is an indication that the F(ii) model is a plausible mechanism for a description of the data. The average values of k_1 and k_{13} were found to be (2.6 ± 0.5) $\times 10^{-10}$ and (3.3 ± 1.4) $\times 10^{-11}$ cm^3 molecule^{-1} s^{-1}, respectively, where the uncertainties are $\pm 1\sigma$.

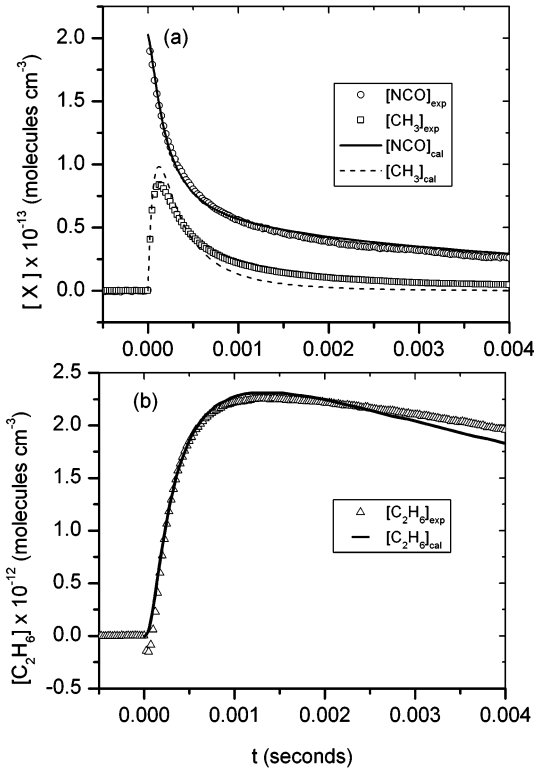

Figure 8. (a) Model F(ii) to fit the C_2H_6 concentration profile by varying k_{11}. Both k_1 and k_{13} were optimized. The experimental data is the same as that given in Figure 3. The optimum value of k_1 was determined to be $(2.3 \pm 0.3) \times 10^{-10}$ cm^3 molecule^{-1} s^{-1}. (b) Same experimental C_2H_6 profile as that depicted in Figure 7b (data points represented by open triangles (Δ)). The optimum value of k_{13} was $(3.5 \pm 0.5) \times 10^{-11}$ cm^3 molecule^{-1} s^{-1}. There is a significant improvement in the agreement between the model predictions and the experimental C_2H_6 profile.

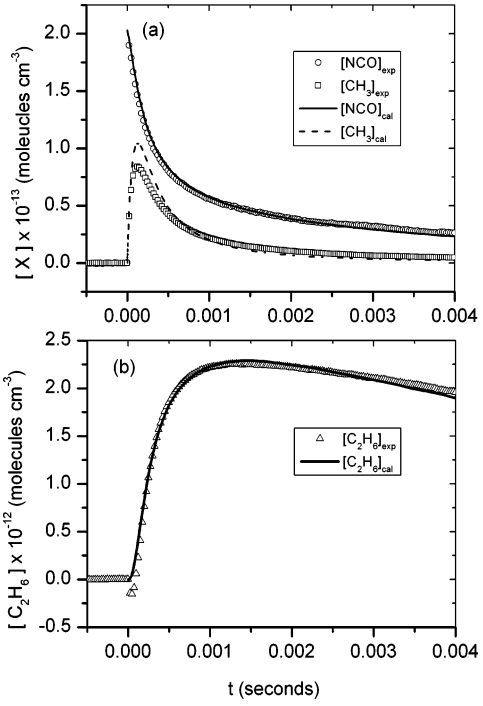

Figure 9. (a) Model F(iii) to fit the C_2H_6 concentration profile by varying k_{11} (see text). For fixed values of k_{10}, k_1 and k_{13} were optimized to fit the NCO and C_2H_6 concentration profiles, respectively. The results shown in Figures 9a and 9b were obtained for $k_{10} = 5.0 \times 10^{-12}$ cm^3 molecule^{-1} s^{-1}. The optimized value of k_1 was $(2.3 \pm 0.3) \times 10^{-10}$ cm^3 molecule^{-1} s^{-1}. (b) Same experimental C_2H_6 profile as that depicted in Figure 7b, but with $k_{10} = 5.0 \times 10^{-12}$ cm^3 molecule^{-1} s^{-1}, the optimum value of k_{13} was $(2.0 \pm 0.3) \times 10^{-11}$ cm^3 molecule^{-1} s^{-1}. There again is an improvement, compared to Figure 8b, in the model predictions and the experimental C_2H_6 profile.

F(iii). Variable Rate Constants k_1 and k_{13} for Fixed Values of k_{10}. Although the F(ii) model provided a better statistical agreement between model predictions and experiment for the CH_3 concentration profiles (i.e., the basic mechanism gave an average mean fraction for the complete data set, $\overline{[CH_3]_{mod}/[CH_3]_{exp}}$, of 1.32 ± 0.06, whereas the F(ii) model reduced this to 1.07 ± 0.53), there was a substantial increase in the scatter for the F(ii) model. The increased scatter was attributed to the loss of CH_3 at long times, as evidenced in Figure 8a, and could be remedied by introducing some chemistry to generate CH_3. There seems to be few possibilities of generating CH_3 outside of the reaction of NCO with a product of reaction 1. The lack of HNCO production placed an upper limit of k_8 of $\sim 2 \times 10^{-16}$ cm^3 molecule^{-1} s^{-1}. Indeed, at long times, there is a slight overprediction of the NCO concentration in model F(ii), compared to the basic model (compare Figures 3 and 8a). To explore the possibility that CH_3 was generated in the system, reaction 10 was added to the reaction mechanism for model F(ii). Preliminary calculations indicated that k_{10} needed to be $\sim 1 \times 10^{-11}$ cm^3 molecule^{-1} s^{-1}. To determine the best values of k_{10}, k_1, and k_{13}, the value of k_{10} was initially set at 2.5×10^{-12}, and incremented in 2.5×10^{-12} cm^3 molecule^{-1} s^{-1} steps while both k_1 and k_{13} were iteratively optimized. The best overall agreement between the model predictions for the [NCO], $[C_2H_6]$, and $[CH_3]$ temporal concentration profiles was obtained for $k_{10} = 5.0 \times 10^{-12}$ cm^3 molecule^{-1} s^{-1}. The corresponding average optimized values of k_1 and k_{13} were $(2.3 \pm 0.5) \times 10^{-10}$ and $(2.5 \pm 1.3) \times 10^{-11}$ cm^3 molecule^{-1} s^{-1}, respectively. The results of the F(iii) model fit to the experimental data given in Figures 3 and 4b are shown in Figure 9. As can be seen in this figure, the agreement between the model predictions and the experimental measurements for the three species NCO, CH_3 and C_2H_6 has improved over the other model treatments. Indeed, this was the case for the complete data set, the F(iii) model provided the best overall agreement. Although the mean of the average fraction, $\overline{[CH_3]_{mod}/[CH_3]_{exp}}$, was 1.36 ± 0.08, almost the same as found in the basic model, the C_2H_6 profiles were fit almost perfectly with a mean average fraction $\overline{[C_2H_6]_{mod}/[C_2H_6]_{exp}}$, of 1.09 ± 0.09. The dependence of k_1 and k_{13} on the initial $[NCO]_0$ was very similar to that for model F(ii) and is not shown.

F(iv). Additional Product Channel (k_{1d}) and Recombination Reaction (k_{15}). Models F(ii) and F(iii) explored the influence of the chemistry between the initially created radicals and possible products of the NCO + CH_3 reaction. There is also the possibility that a reaction or series of reactions of a product from reaction 1 generated C_2H_6 but did not necessarily react with NCO or CH_3. To investigate this scenario, the basic reaction mechanism was modified by the addition of a fourth product channel for reaction 1, giving $CH_3N(X^3A_2'') + CO$ and reaction 15, the recombination of CH_3N to form C_2H_6 and N_2. Using the $\Delta H_{f,0}$ values in Table 3, the reaction enthalpy for channel 1d is predicted to be −32 kJ/mol. Although there is some uncertainty in the heat of formation[43] of $CH_3N(X^3A_2'')$, the reaction exothermicity is small enough that the energy available to the products is well below the excited singlet $CH_3N(a^1A_1)$ state and an isomerization barrier on the triplet surface.[43,56] The addition of channel 1d and reaction 15 to the basic reaction mechanism does not perturb the NCO or

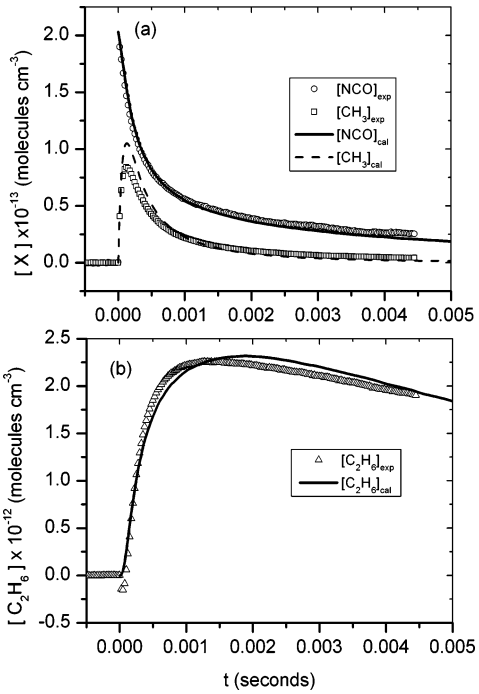

Figure 10. (a) Model F(iv) to fit the C_2H_6 concentration profile by varying k_{11} (see text). Same fits as those given in Figure 3. (b). Same experimental C_2H_6 profile as that depicted in Figure 7b, except with $k_{1d} = 4.3 \times 10^{-11}$ cm^3 molecule^{-1} s^{-1} and k_{15} was optimized to fit the C_2H_6 experimental profile. For this case, the optimum value of k_{15} was $(2.1 \pm 0.8) \times 10^{-10}$ cm^3 molecule^{-1} s^{-1}.

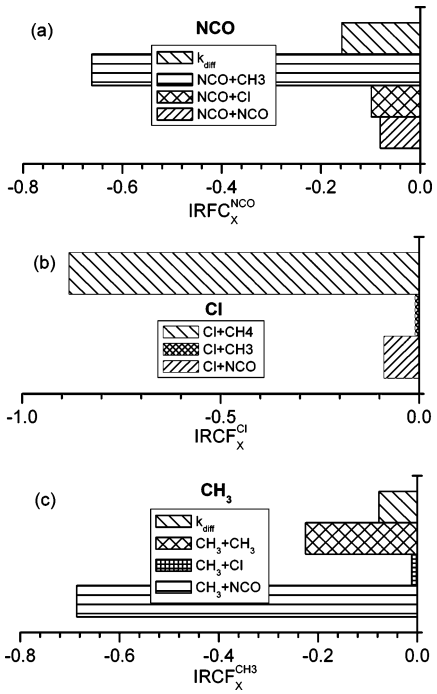

Figure 11. Integrated reaction contribution factors (IRCFs), expressed as a fraction for the removal of NCO, CH_3, and Cl for the experiment illustrated in Figure 3. The IRCFs were calculated using the basic reaction mechanism in Table 2 with the optimum value of k_1 equal to 1.7×10^{-10} cm^3 molecule^{-1} s^{-1}. Note that reaction 1 accounts for the removal of ~70% of the NCO and CH_3 radical pools, and reaction 2 accounts for the removal of ~90% of the Cl atoms.

CH_3 concentration profiles, so that k_1 was the same as that observed in the basic mechanism. The branching fraction into channel 1d was varied from 25% to 100% in steps of 25%. At each step, the optimized value of k_{15} was determined by fitting the C_2H_6 temporal concentration profile. The best agreement between the model predictions and experiment was observed for k_{1d} to be 25% of k_1. The results for the experiment shown in Figures 3 and 4b, analyzed using the F(iv) model, are presented in Figure 10. As can be seen from Figure 10b, the F(iv) model provided a reasonable fit to the C_2H_6 concentration profile. For this case, the value of k_{1d} was 4.3×10^{-11} cm^3 molecule^{-1} s^{-1}, and the optimized value of k_{15} was found to be $(2.0 \pm 0.8) \times 10^{-10}$ cm^3 molecule^{-1} s^{-1}. The results from the analysis of all the experimental runs are shown in Figure 6d plotted as a function of the initial NCO concentration. As is evident from Figure 6d, there is a strong dependence of k_{15} on the initial NCO concentration, indicating that model F(iv) does not provide an appropriate description of the complete data set.

G. Reaction Contribution Factor Analysis. In the determination of kinetic rate constants from chemical model simulations, it is helpful to have a measure of the contribution each reaction makes to the overall removal or production of species in the model. A reaction contribution factor analysis is particularly useful in this regard,[57] especially under the current conditions, where both concentration and rate constants measurements are important. The reaction contribution factor at time t, for species i removed by reaction with species j ($RCF^i_j(t)$), which is given by $RCF^i_j(t) = -k_{ij}$[I][J], or produced in reaction between species l and m, RCF^i_{lm}, which is given by $RCF^i_{lm} = k_{lm}$[L][M]. The corresponding integrated reaction contribution factor ($IRCF^i_{j/lm}$) from time $t = 0$ to time t is the total flux of species i that is removed in reaction with species j or produced in reaction between species l and m, respectively, up to time t.

An example of the IRCF treatment for the basic mechanism analysis of the experimental data in Figure 3 is presented in Figure 11. Similar analyses were performed for each reaction model and experimental run. In Figure 11, the $IRCF^X$ values for $t = 5$ ms, where X is NCO, CH_3, and Cl, are plotted as fractions of the total flux for removal or production of each species. Only $IRCF^X$ fractions, with values >0.01, are plotted in the figures. Note that for the species, NCO, CH_3, and Cl, the most important reaction for removal is the one of most interest according to the model; thus, determination of k_1 and k_2 should not depend strongly on other rate processes. For NCO, loss by diffusion is the second most important loss mechanism, Figure 11a, and for Cl, k_3 accounted for 10% of the total removal of Cl atoms, Figure 11b. Even for CH_3, reaction 1 accounted for 69% of the total removal of CH_3, while reaction 11 accounted for just over 20%.

The IRCF analysis shown in Figure 11 was representative of the complete data set. For the reaction models F(i), F(ii), and F(iii), the increased production of C_2H_6 was from reactions removing CH_3. However, the introduction of these new losses of CH_3 accounted for only a relatively small fraction of the total CH_3 radical-flux loss of 5%−10%; nevertheless, this caused a much larger fractional increase in the optimized k_1 values of 20%−30%, as shown in Figure 6.

H. Theoretical Estimate of Bond Dissociation Energies. No experimental information on the bond dissociation energy of CH_3NCO and its isomers could be found, so theoretical calculations were performed to evaluate these quantities and their equilibrium rotational and vibrational properties. This information was used in a theoretical estimate of the recombination rate constant into the CH_3NCO and CH_3OCN products and will be discussed in the next section. The electronic structure calculations were performed on a Dell Xeon PC using a commercial program (HyperChem[58]). The calculations were

TABLE 5: Theoretical Estimates of the Bond Energies and Morse Parameters (β) for the Dissociating Bond, H_3C-NCO and H_3C-OCN, of the Energetically Accessible Isomers of CH_3NCO

isomer	dissociation energy,[a] (X^1A') (kJ/mol)	β^1 ($Å^{-1}$)[b]	ν^1_D (cm^{-1})[c]	dissociation energy,[a] (a^3A'') (kJ/mol)	β^3 ($Å^{-1}$)[b]	ν^3_D (cm^{-1})[c]
CH_3NCO	356	1.826	747	58	5.439	885
CH_3OCN	226	2.521	907	(188)[d]		

[a] Defined for X → CH_3 + NCO. Calculated at the DFT-B3LYP/6-311++G** level of theory and corrected for zero-point energy. [b] Vibrational frequencies were calculated at a lower level of theory, MP2/6-311G**. [c] Calculated vibrational frequencies corrected by a factor 0.92. [d] Above the CH_3 + NCO energy asymptote.

performed at the DFT-B3LYP/6-311G**, 6-311++G** or aug-vpdz/ccvpdz level of theory. All three basis sets gave similar results, with the reported dissociation energies calculated using the 6-311++G** basis set. Comparison of calculated bond energies at the same level of theory to known values for related compounds (NCO and HNCO)[36] suggested that the accuracy of the calculations was probably ±30 kJ/mol. Of the six isomers of CH_3NCO that involve rearrangement of the atoms in the NCO moiety, those that involve the cyanato (NCO) and fulminato (CNO) structures have potential energy minima below the NCO + CH_3 asymptote. The two methylcyante isomers (CH_3NCO and CH_3OCN) can form from NCO + CH_3 reactants without any energy barrier along the reaction coordinate. The formation of the other isomers requires significant activation energies, because of the necessity of breaking and reforming the various bonds in the NCO moiety. There is also the possibility of formation of some of these isomers on the excited singlet or triplet PESs. The theoretical calculations could only be performed on the lowest energetic PES in the singlet and triplet manifolds, (X^1A') and (a^3A''), respectively.

The results for the theoretical calculations for the bond energies of the energetic possible CH_3-NCO recombination products are summarized in Table 5. The calculations of $k_{rec\infty}$, to be discussed in the section IV.B, required a Morse potential energy description of the newly formed bond. The Morse parameter, $\beta = \sqrt{2\pi^2\mu/Dh^2}\ \nu_D$ (where D is the bond dissociation energy and ν_D is the vibrational frequency in wavenumbers of the new bond), is also reported in Table 5.

IV. Discussion

A. Products of NCO + CH_3. HCN or HNC were the only detected species attributed to be products of reaction 1. It was assumed that the co-product of both channels was H_2CO. However, as discussed in section III.E, there was only modest agreement between the model calculations and the experimental observations for these species. In any case, these two channels accounted for only 0.6% of the total products.

Attempts were made to detect the species NH_2, H_2CO, and CH_3N, but these attempts were unsuccessful. The exploration for H_2CO and CH_3N lines encompassed the spectral region from ~3.30 μm to 3.36 μm. In the case of H_2CO and CH_3N, this failure could be attributed to spectral congestion due to CH_4 and C_2H_6 absorptions, particularly if these species were produced as minor products, which likely seems to be the case. The small concentration of detected secondary species suggests that the recombination products CH_3NCO and CH_3OCN are dominant.

Both NCO + CH_3 and C_2H_3 + NO are energy asymptotes on the global C_2-H_3-N-O PES and may be referenced to the energy landscape of Figure 1 of Zou et al.,[14] using Tables 2 and 5 to calculate the $\Delta H_{f,0}$ value for the CH_3 + NCO and CH_3NCO asymptotes to be at 278 kJ/mol and −78 kJ/mol, respectively. These features are 116.6 kJ/mol below the C_2H_3 + NO asymptote and 102 kJ/mol below the H_2CO + HCN asymptote, respectively. Sumathi et al.[12] calculated that CH_3NCO was 130 kJ/mol less energetic than H_2CO + HCN. This is consistent with the difference in the theoretical calculations. At the MP2/6-311++G(p,d) level of theory, Sumanthi et al.[12] provided a global view of the energy landscape on the C_2-H_3-N-O PES. These workers found that the only bimolecular product channels for the C_2H_3 + NO reaction were CH_2NH + CO, CH_2O + HCN, and CH_2O + HNC. These products emanated from the bound C_2H_3NO adduct through reaction paths that had higher barriers than the CH_3 + NCO energy asymptote. At higher levels of theory, Striebel et al.[13] found lower energetic pathways from the CH_3NO adduct through an 1,2-oxazete intermediate leading to the HCN + H_2CO product channel. Zou et al.[14] extended these calculations to include another low-energy pathway from the C_2H_3NO adduct to the CH_2NH + CO product channel. However, even these new low-energy pathways have energy maxima lying substantially above the CH_3 + NCO asymptote; hence, the known features of the global C_2-H_3-N-O PES cannot describe bimolecular product formation in the NCO + CH_3 reaction.

B. High-Pressure Recombination Rate Constants. The dominant reaction channel for reaction 1 seems to be recombination; however, the measured value of k_1 is larger than most molecular radical recombination reactions. A theoretical description of the recombination reactions would help in understanding the reaction dynamics of the NCO + CH_3 system. Troe's formulation[15] for $k_{rec,\infty}$ is a useful approximate method for estimating unimolecular and recombination rate constants. Furthermore, this formulation has been useful in characterizing the pressure dependence of unimolecular reaction rate constants[59] and has been successful in predicting the values of recombination rate constants under both high-pressure[60] and low-pressure[61] conditions. The only information necessary to implement the calculation of $k_{rec,\infty}$ is the equilibrium structure and vibrational frequencies of the dissociating molecule AB, the bond energy of A−B, a Morse potential energy description of the A−B bond, and a value for the interpolation parameter α, which describes how the transitional modes evolve into the rotational motion of the radical fragments. The high-pressure recombination rate constant for A + B → A is given by

$$k_{rec,\infty} = \frac{kT}{h}\left(\frac{h^2}{2\pi kT}\right)^{3/2} \frac{Q_{el}(AB)}{Q_{el}(A)Q_{el}(B)} \frac{Q^*_{cent}\, F^*_{AMe}(1/\sigma^*)}{Q_{vr}(A)Q_{vr}(B)} \prod^{r} Q^*_j \prod^{b} Q^*_m \exp\left(-\frac{\Delta E_{0z}}{kT}\right) \quad \text{(E5)}$$

where k, h, and T have their usual meaning, μ is the reduced mass, $Q_{el}(X)$ is the electronic partition function of X, Q^*_{cent} is a centrifugal pseudo-partition function, F^*_{AMe} is a factor that corrects for the rotation character of the disappearing oscillators, σ^* is the effective symmetry number at the transition state, $Q_{vr}(X)$ is the rovibrational partition function of X, Q^*_j is the vibrational partition function for the conserved modes of AB, Q^*_m is the vibrational partition function for the transitional modes, and ΔE_{0z} is the lowest threshold energy for recombination.

Four isomers of CH_3NCO have potential minima below the NCO + CH_3 asymptote on the global C_2-H_3-N-O PES.[12]

TABLE 6: Estimates for $k_{rec,\infty}$ Producing CH_3NCO/CH_3NCO (X^1A') Isomers at 300 K

isomeric product	$k_{rec,\infty}$ (cm^3 $molecule^{-1}$ s^{-1})		
	$\alpha/\beta = 0.46$	$\alpha/\beta = 0.55$	$\alpha/\beta = 0.37$
CH_3NCO	1.10×10^{-11}	3.8×10^{-11}	3.4×10^{-12}
CH_3OCN	2.5×10^{-12}	9.8×10^{-12}	6.6×10^{-13}

Only CH_3NCO and CH_3OCN can form in simple recombination reactions from NCO + CH_3 reactants. The $CH_3NCO(a^3A'')$ was determined to be weakly bound, as reported in Table 5. However, the $CH_3NCO(a^3A'')$ PES likely has similar topology as the $HNCO(a^3A'')$ PES, where there is a substantial barrier for bound $HNCO(a^3A'')$ to dissociation to H + NCO products.[62,63] Thus, direct recombination into $CH_3NCO(a^3A'')$ is unlikely at low temperatures.

The comparison of calculated $k_{rec\infty}$ values to experimental values requires a determination of α. This is usually done by comparison with other systems. In a systematic study, Cobos and Troe[60] determined that values of α/β equal to 0.46 ± 0.09 correlated the calculated and experimental values of $k_{rec\infty}$ for over 26 systems. The calculated values of $k_{rec\infty}$ for each methylcyanate isomer are reported in Table 6, using this range of α.

Using the basic mechanism (section III.E), the value of k_1 was determined to be 2.1×10^{-10} cm^3 $molecule^{-1}$ s^{-1}. This is a factor of 4 larger than the combined theoretical estimate in Table 6 for recombination into the methylcyante products for $\alpha/\beta = 0.55$ and is ~15 times larger if $\alpha/\beta = 0.46$. Neither methylcyante isomer is unusual, compared to the systems studied by Cobos and Troe, so this range of α/β should provide a reasonable estimate of the theoretical value of $k_{rec\infty}$ and cannot account for the experimental value of k_1. There seems to be another pathway that is responsible for the reaction between NCO + CH_3. As discussed in section IV.A, the known reaction pathways on the C_2-H_3-N-O PES cannot contribute to product formation starting from the NCO + CH_3 asymptote. A possible explanation for the observed value of k_1 is the participation of the excited singlet electronic states of the methylcyanate isomers. Using similar calculations, Smith[4] showed that excited electronic states could participate in recombination processes. Further exploration of the C_2-H_3-N-O PES and more-accurate calculations of $k_{rec\infty}$ will be needed to verify this speculation.

C. Estimated Uncertainties in k_1. The determination of k_1 requires that the concentrations of both NCO and CH_3 be determined. Although both species were monitored, the determination of k_1 used only the NCO profile and the radical concentration determined by the maximum in the HCl concentration profile, as discussed in section III.E. The uncertainty in the determination of σ_{pk}^{NCO} was ±4% (Table 1) and produced a corresponding uncertainty in k_1. The large uncertainty in $\sigma_{pk}^{CH_3}$ (Table 1), and the apparent missing chemistry involving the CH_3 radical (section III.F), precluded the use of this radical in the direct determination of k_1. The random scatter in the measurements of k_1 contributed ±19% to the uncertainty of k_1 (see section III.E).

The main reason to explore the different reaction mechanisms outlined in section III.F was to determine the influence an unknown chemistry could have on the evaluation of k_1. As summarized in Figure 6, k_1 varied from 2.1×10^{-10} cm^3 $molecule^{-1}$ s^{-1} using the basic reaction mechanism (Table 2) to 2.7×10^{-10} cm^3 $molecule^{-1}$ s^{-1} for model F(i). The other applicable models gave k_1 values closer to the basic mechanism value, and an estimate of the influence of the missing chemistry on k_1 was taken to be +20%. The k_1 value that was determined using the basic mechanism was considered a lower limit.

As in previous work,[5,10,11] the fractional IRCF for a particular reaction multiplied by the uncertainty in the rate constant for that process was considered to be representative of the uncertainty that reaction had on the determination of k_1. For both NCO and CH_3, diffusion was a significant removal process, and the uncertainty in k_{diff}^{NCO/CH_3} was estimated to be ±20%, which is approximately twice the experimental scatter in the determination of the diffusion rate constants for the stable species. The uncertainties in the various rate constants are listed in Table 2. For NCO, the accumulated uncertainty from the errors in the rate constants input into the basic mechanism was ±12%, with half of this uncertainty coming from reaction 3 for which the uncertainty included both absolute and random errors. For CH_3, the accumulated uncertainty was ±4%, with diffusion accounting for half of the uncertainty. Thus, the total uncertainty introduced by an estimate of the errors to the rate constants in the basic model was estimated to be ±16%.

Overall, the total uncertainty in the determination of k_1 was the sum of the four sources of error and was determined to be +60% and −40%, including systematic and random error.

V. Summary

The rate constant for the NCO + CH_3 reaction was measured to be $(2.1 \pm 0.8(1.3)) \times 10^{-10}$ cm^3 $molecule^{-1}$ s^{-1} at 293 ± 2 K, where the error bars are an estimate of the absolute and random experimental errors at the 68% confidence level. The measurements were performed in an excess of CH_4 over the pressure range of 2.8−4.5 Torr. The rate constant for the reaction Cl + CH_4 was also measured to be $(9.2 \pm 0.2) \times 10^{-14}$ cm^3 $molecule^{-1}$ s^{-1} at 293 ± 2 K, where the error is ±1σ. The only species that could be attributed to be products of the NCO + CH_3 reaction were HNC and HCN: the co-product of both channels was assumed to be H_2CO. The appearance rate of both channels was faster than model predictions. The branching fraction, as a percentage, into these channels was 0.22% ± 0.09% and 0.39% ± 0.24%, for HNC + H_2CO and HCN + H_2CO, respectively, where the uncertainty is the accumulative random error only (±1σ).

The NH radical was also observed in these experiments; however, the source of this species was not reaction 1. NH was speculated to be produced from the reaction of electronically excited $N(^2D)$ atoms with CH_4 (see section III.E). If this is the case, the rate constant for the reaction $N(^2D) + CH_4 \rightarrow CH_3 +$ NH was measured to be $(9.7 \pm 1.4) \times 10^{-13}$ cm^3 $molecule^{-1}$ s^{-1}, where the uncertainty is ±1σ.

The complete data set was analyzed using five different reaction mechanisms, which are summarized in Table 2 and sections III.E and III.F. The temporal concentration profiles of C_2H_6 were recorded in these experiments, so that its production in the $CH_3 + CH_3$ recombination reaction was monitored. The basic reaction mechanism was not successful at completely reproducing the CH_3 and C_2H_6 profiles. The calculated CH_3 profiles consistently overestimated the peak CH_3 concentration and the calculated C_2H_6 profiles consistently underestimated the experimental C_2H_6 concentration. These discrepancies were greater than the uncertainties in the species absorption coefficients and suggested that there was some chemistry missing from the basic mechanism. Four different reaction sequences were considered and explored the effects different reactions exerted on the determination of k_1. Much improved agreement between calculated and experimental CH_3 and C_2H_6 profiles

was obtained in models in which CH_3 reacted with a product of reaction 1 to produce C_2H_6 (see sections III.F(ii) and III.F(iii)).

The possibility of bimolecular channel products was examined from the perspective of known features of the global C_2-H_3-N-O potential energy surface (PES);[12−14] however, reaction pathways to known bimolecular products are not energetically accessible from the NCO + CH_3 asymptote. This suggested that the main product channel of reaction 1 was recombination, forming CH_3NCO and CH_3OCN. Theoretical estimates of $k_{rec,\infty}$ for each channel (Table 6) were conducted using eq E5. The calculations indicated that direct recombination, forming ground-state singlet products, could not account for the observed k_1 value. Either unknown disproportionation channels or the participation of excited electronic states could explain the experimental measurement of k_1.

Acknowledgment. This work was supported by the U. S. Department of Energy, Office of Basic Energy Sciences, Division of Chemical Sciences, Geosciences, and Biosciences (under Contract No. W-31-109-ENG-38).

References and Notes

(1) Truhlar, D. G.; Garret, B. C.; Klippenstein, S. J. *J. Phys. Chem.* **1995**, *100*, 12771.
(2) Graff, M. M.; Wagner, A. F. *J. Chem. Phys.* **1990**, *92*, 2423.
(3) Klippenstein, S. J.; Harding, L. B. *J. Phys. Chem.* **1999**, *103*, 9388.
(4) Smith, I. M. M. *Int. J. Chem. Kinet.* **1984**, *16*, 423.
(5) Gao, Y.; Macdonald, R. G. *J. Phys. Chem.* **2005**, *109*, 5388.
(6) Miller, J. A.; Bowman, C. T. *Prog. Energy Combust. Sci.* **1989**, *15*, 287.
(7) Gardiner, W. C., Jr. *Gas-Phase Combustion Chemistry*; Springer−Verlag: New York, 1999.
(8) Hughes, K. J.; Turanyi, T.; Clague, A. R.; Pilling, M. J. *Int. J. Chem. Kinet.* **2001**, *33*, 513.
(9) Pilling, M. J.; Stocker, D. W. *Annu. Rep. Prog. Chem., Sect. C* **1999**, *95*, 277.
(10) Gao, Y.; Macdonald, R. G. *J. Phys. Chem. A* **2003**, *107*, 4625.
(11) Decker, B. K.; Macdonald, R. G. *J. Phys. Chem. A* **2003**, *107*, 9137.
(12) Sumathi, R.; Nguyen, H. M. T.; Nguyen, M. T.; Peeters, J. *J. Phys. Chem. A* **2000**, *104*, 1905.
(13) Striebel, F.; Jusinski, L. E.; Fahr, A.; Halpern, J. B.; Klippenstein, S. J.; Taatjes, C. A. *Phys. Chem. Chem. Phys.* **2004**, *6*, 2216.
(14) Zou, P.; Klippenstein, S. J.; Osborn, D. L. *J. Phys. Chem. A* **2005**, *109*, 4921.
(15) Troe, J. *J. Chem. Phys.* **1981**, *75*, 226.
(16) He, G.; Tokue, I.; Harding, L. B.; Macdonald, R. G. *J. Phys. Chem. A* **1998**, *102*, 7653.
(17) Kroto, H. W.; *Molecular Rotational Spectra*; Dover: New York, 1992.
(18) Bethardy, G. A.; Macdonald, R. G. *J. Chem. Phys.* **1995**, *103*, 2863.
(19) Pine, A. S.; Fried, A.; Elkins, J. W. *J. Mol. Spectrosc.* **1985**, *109*, 30.
(20) Smith, M. A. H.; Harvey, G. L.; Pellet, G. L. *J. Mol. Spectrosc.* **1984**, *105*, 105.
(21) Mourik T.; Harris G. J.; Polyansky, O. L.; Tennyson J.; Császár A. G.; Knowles, P. J. *J. Chem. Phys.* **2001**, *115*, 3706.
(22) He, G.; Macdonald, R. G. *Chem. Phys. Lett.* **1999**, *301*, 175.
(23) Chackerian, C., Jr.; Guelachvili, G.; López-Piñerio, A.; Tipping, R. H. *J. Chem Phys.* **1989**, *90*, 641.
(24) Cantarella, E.; Culot, F.; Liévin, J. *Phys. Scr.* **1992**, *46*, 489.
(25) Macdonald, R. G. Manuscript in preparation.
(26) Pine, A. S.; Stone, S. C. *J. Mol. Spectrosc.* **1996**, *175*, 21.
(27) Pilgrim, J. S.; McIlroy, A.; Taatjes, C. A. *J. Phys. Chem A* **1997**, *101*, 1873.
(28) Bryukov, M. G.; Slagle, I. R.; Knyazwv, V. D. *J. Phys. Chem. A* **2002**, *102*, 10525.
(29) Parker, J. K.; Payne, W. A.; Cody, R. J.; Nesbitt, F. L.; Stief, l. J.; Klippenstein, S. J.; Harding, L. B. Submitted to *J. Phys. Chem. A.*
(30) Linstrom, P. J., Mallard, W. G., Eds. *NIST Chemistry WebBook, NIST Standard Reference Database*, Number 69; National Institute of Standards and Technology (NIST): Gaithersburg, MD, 2003 (http://webbook.nist.gov).
(31) Wategaonkar, S.; Setser, D. W. *J. Phys. Chem.* **1993**, *97*, 10028.
(32) Park, J.; Hershberger, J. F. *Chem. Phys. Lett.* **1994**, *218*, 537.
(33) Becker, K. H.; Geiger, H.; Schmidt, F.; Wiesen, P. *Phys. Chem. Chem. Phys.* **1999**, *1*, 5305.
(34) Slagle, I. R.; Gutman, D.; Dacies, J. W.; Pilling, M. J. *J. Phys. Chem.* **1988**, *92*, 2455.
(35) Clyne, M. A. A.; MacRobert, A. J. *J. Chem. Soc., Faraday Trans. 2* **1983**, *79*, 283.
(36) Schuurman, M. S.; Muir, S. R.; Allen, D. W.; Schaefer, H. F., III. *J. Chem. Phys.* **2004**, *120*, 11586.
(37) Ruscic, B.; Boggs, J. E.; Burcat, A.; Császár, A. G.; Demaison, J.; Janoschek, R.; Martin, J. M. L.; Morton, M. L.; Rossi, M. J.; Stanton, J. F.; Szalay, P. G.; Westmoreland, P. R.; Zabel, F.; Bérces, T. *J. Chem. Ref. Data* **2005**, *34*, 573.
(38) Dixon, D. A.; Feller, D.; Peterson, K. A. *J. Chem. Phys.* **2001**, *115*, 2576.
(39) Xantheas, S. S.; Dunning, T. H., Jr.; Mavridis, A. *J. Chem. Phys.* **1997**, *106*, 3280.
(40) Berkowitz, J.; Ellison, B. E.; Gutman, D. *J. Phys. Chem.* **1994**, *98*, 2744.
(41) Ruscic, B.; Pinzon, R. E.; Morton, M. L.; Laszevski, G.; Bittner, S. J.; Nijsure, S. G.; Amin, K. A.; Minkoff, M.; Wagner, A. F. *J. Phys. Chem. A* **2004**, *108*, 9979.
(42) Gurvich, L. V.; Veyts, I. V.; Alcock, C. B. *Thermodynamic Properties of Individual Substances*; Fourth Edition; Hemisphere Publishing Company: New York, 1989.
(43) Gonzalez, C.; Schlegal, H. B. *J. Am. Chem. Soc.* **1992**, *114*, 9122.
(44) Press: W. H.; Flannery, B. P.; Teukolsky, S. A.; Vetterling, W. T. *Numerical Recipes: The Art of Scientific Computing*; Cambridge University Press: Cambridge, U.K., 1986.
(45) Astbury, C. J.; Hancock, G.; McKendrick, K. G. *J. Chem. Soc., Faraday Trans.* **1993**, *89*, 405.
(46) Fernandez, J. A.; Puyuelo, P.; Husain, D.; Rayo, M. N. S.; Castaño, F. *J. Chem. Phys.* **1997**, *106*, 7090.
(47) Fuller, E. N.; Ensley, K.; Giddings, J. C. *J. Phys. Chem.* **1969**, *73*, 3679.
(48) Reid, R. C.; Prausnitz, J. M.; Poling, B. E. *The Properties of Gases and Liquids*; McGraw−Hill: New York, 1989.
(49) Hirschmann, R. P.; Kniseley, R. N.; Fassel, V. A. *Spectrochim. Acta* **1965,** *21*, 2125.
(50) Pasinszki, T.; Westwood, N. P. C. *J. Phys. Chem. A* 1**995**, *99*, 1649.
(51) Cannon, B. D.; Francisco, J. S.; Smith, I. W. M. *Chem. Phys.* **1984**, *89*, 141.
(52) Smith, I. W. M.; Warr J. F. *J. Chem. Soc., Faraday Trans*. **1991**, *87*, 807.
(53) Bell, D. D.; Coombe, R. D. *J. Chem. Phys.* **1985**, *82*, 1317.
(54) Kurosaki, Y.; Takayanagi, T.; Sato, K.; Tsunashima, S. *J. Phys. Chem. A* **1998**, *102*, 254.
(55) Takayanagi, T.; Kurosaki, Y.; Sato, K.; Misawa, K.; Kobayashi, Y.; Tsunashima, S. *J. Phys. Chem. A* **1999**, *103*, 250.
(56) Richards, C., Jr.; Meredith, C.; Kim, S.-J.; Quelch, G. E.; Schaefer, H. F., III. *J. Chem. Phys.* **1994**, *100*, 481.
(57) Warnatz, J.; Maas, U.; Dibble, R. W. *Combustion: Physical and Chemical Fundamentals, Modeling and Simulation, Experiments, Pollutant Formation*; Springer: Berlin, 1995.
(58) HyperChem. Hypercube, Inc.: Gainesville, FL, 32601.
(59) Gilbert, R. G.; Luther, K.; Troe, J. *Ber. Bunsen−Ges. Phys. Chem. Chem. Phys.* **1983**, *87*, 169.
(60) Cobos, C. J.; Troe, J. *J. Chem. Phys.* **1985**, *83*, 1010.
(61) Patrick, R.; Golden, D. M. *Int. J. Chem. Kinet.* **1983**, *15*, 1189.
(62) Mebel, A. M.; Morokuma, M. C. *J. Chem. Phys*. **1996**, *105*, 6439.
(63) Kaledin, A. L.; Cui. Q.; Heaven, M. C.; Morokuma, K. *J. Chem. Phys.* **1999**, *111*, 5004.